RESEARCH ARTICLE

ADVANCED FUNCTIONAL MATERIALS
www.afm-journal.de

Universal Core–Shell Nanowire Memristor Platform with Quasi-2D Filament Confinement for Scalable Neuromorphic Applications

Enxiu Wu, Yue Wang, Shida Huo, Junxi Xu, Ming Sheng, Hongsheng Liu, Li Zhong, Junfeng Gao,* Yuan Xie,* and Caofeng Pan**

Memristors are central to the advancement of nano-electronic and neuromorphic systems due to their fast-switching speed, low power consumption, and compatibility with CMOS technology. However, the stochastic formation of conductive filaments (CFs) in filament-based memristors remains a major obstacle, leading to significant variability in switching performance. Here, a novel memristor architecture that combines spatial confinement precision with fabrication simplicity is proposed; a core–shell silver nanowire structure, consisting of a highly conductive Ag core wrapped in a polyvinylpyrrolidone (PVP) shell. This 1D nanowire serves both as the active electrode and as a geometric scaffold that constrains CF growth within a quasi-2D plane. The resulting device demonstrates excellent electrical performance, including a low threshold voltage (0.22 V), high switching uniformity (coefficient of variation <15%), and ultra-low power consumption (≈400 pW). Molecular dynamics simulations reveal the spontaneous rupture behavior of CF and establish a correlation between filament dimensions and their temporal stability. Furthermore, the system emulates key nociceptor-like functionalities—such as threshold triggering, relaxation recovery, and sensitization—highlighting its neuromorphic potential. This work establishes a versatile structural platform for precise nanoscale CF control using a structurally simple core–shell nanowire architecture, offering broad applicability across device formats for energy-efficient, neuromorphic-compatible memristive electronics.

1. Introduction

Memristors have emerged as a key enabling technology in advanced nanoelectronics and neuromorphic computing due to their high speed, scalability, low power consumption, and compatibility with CMOS processes.[1–4] Among various memristor types, devices based on the migration of reactive species (e.g., silver atoms, oxygen ions, vacancies) and the formation of conductive filaments (CFs) in dielectric layers have shown the most rapid progress.[5–8] However, accurately controlling the position and number of these filaments remains a critical challenge, resulting in substantial variability in switching thresholds.

To mitigate this issue, spatial confinement strategies have been proposed to guide CF formation along predefined paths, thereby enhancing switching uniformity. One promising route is employing one-dimensional (1D) nanowire planar structures to guide filament growth along a defined path.[9–14] While 1D-structured memristors offer enhanced filament

---

E. Wu, Y. Wang, S. Huo, J. Xu
State Key Laboratory of Precision Measurement Technology and Instruments
School of Precision Instruments and Opto-electronics Engineering
Tianjin University
Tianjin 300072, P. R. China
E-mail: enxiuwu@tju.edu.cn

M. Sheng, L. Zhong
SEU-FEI Nano-Pico Center
Key Laboratory of MEMS of Ministry of Education
School of Integrated Circuits
Southeast University
Nanjing 210096, China

H. Liu, J. Gao
Key Laboratory of Materials Modification by Laser
Ministry of Education
School of Physics
Ion and Electron Beams (Dalian University of Technology)
Dalian 116024, China
E-mail: gaojf@dlut.edu.cn

Y. Xie
School of Electronics and Information Engineering
Tiangong University
Tianjin 300387, P. R. China
E-mail: xieyuan@tiangong.edu.cn

C. Pan
Institute of Atomic Manufacturing
Beihang University
Beijing 100191, P. R. China
E-mail: pancaofeng@buaa.edu.cn

C. Pan
International Research Institute for Multidisciplinary Science
Beihang University
Beijing 100191, China

The ORCID identification number(s) for the author(s) of this article can be found under https://doi.org/10.1002/adfm.202518764

DOI: 10.1002/adfm.202518764

confinement and tunability, filaments formed via oxygen vacancy migrationoften exhibit excessive length,[15–18] leading to high power consumption and slower switching speed. Additionally, internal defects and environmental fluctuations introduce reliability issues.[19–24] Other employ strategies which constrain the growth area using tailored electrode geometries or interface modifications.[17,25–29] For instance, vertically stacked structures with reduced electrode overlap confine the conductive region into a smaller volume.[30–32] Dang et al. introduced a mortise-tenon-shaped (MTS) architecture, embedding h-BN into the HfO_2 switching layer to localize filament growth, achieving improved device consistency with only 2.5% cycle-to-cycle and 6.9% device-to-device variation.[33] Similarly, Li et al. designed nano-cone electrodes to control the nucleation and growth of silver filaments, thereby reducing stochastic variability.[34] While these structures can effectively improve CF localization and consistency, their fabrication often requires precise patterning, multi-step deposition, or material integration strategies, increasing the overall manufacturing complexity and limiting scalability.

To address these limitations, we propose a novel yet fabrication-friendly strategy: the integration of a 1D metal nanowire as an active electrode to confine CF growth within a quasi-2D plane. This approach simplifies the device architecture while maintaining high spatial control over filament formation.

In this work, we report a high-performance memristor based on a core–shell silver nanowire, comprising a highly conductive silver core and an ultrathin polyvinylpyrrolidone (PVP) shell. The PVP layer not only stabilizes the nanowire formation but also serves as an ultrathin dielectric interface that bridges interfacial defects. The complete device structure—metal/ultrathin dielectric/1D metal nanowire—demonstrates excellent electrical characteristics: a low threshold voltage (0.22 V), consistent switching behavior (coefficient of variation <15%), and ultra-low switching power consumption (≈400 pW). Furthermore, the device exhibits both volatile and nonvolatile switching modes, expanding the range of applications. Molecular dynamics simulations reveal the dynamics of spontaneous conductive filament rupture in the absence of an electric field and establish the correlation between filament size and lifetime. Additionally, the system replicates essential features of biological nociceptors, such as threshold-triggered response, relaxation recovery, and sensitization—demonstrating the potential of this structure for neuromorphic applications. This work presents a generalizable strategy for deterministic CF confinement that integrates high spatial precision with manufacturing simplicity. By utilizing a 1D nanowire-based core–shell design, it establishes a universal platform applicable to a wide range of switching materials and device geometries, advancing the scalable design of low-power, bioinspired memristive electronics.

2. Results and Discussion

The 1D silver nanowire electrode confines CF growth within the vertical plane via nanoscale structural confinement. This spatial confinement suppresses stochastic CF formation, thereby stabilizing threshold voltage (V_{th}) distribution (**Figure** 1a). The stochastic formation of conductive filaments between planar metal electrodes induces significant threshold voltage fluctuations. In contrast, implementing 1D metallic electrodes suppresses V_{th} variation substantially while simultaneously reducing the absolute V_{th} value (Figure 1b). Structural characterization confirms that the nanowire comprises a metallic Ag core coated with PVP,[35,36] forming a core–shell configuration (Figure 1c). This organic encapsulation layer, as revealed by energy-dispersive X-ray spectroscopy (EDS) and TEM (Figure 1d,e). Additional physical characteristics of the nanowire devices can be found in Figure S1 (Supporting Information). In previous studies, PVP functions not only as a surface stabilizer[37] but also as a functional tunneling layer, enabling memristive behavior in the vertical configuration.[38]

The switching behavior of this device originates from the nanoscale electrode-nanowire junction. As schematized in **Figure** 2a, equally spaced Au electrodes (denoted A, B, C from left to right) align parallel to the silver nanowire. Through unidirectional voltage scanning applied across the two gold electrodes (A and B) on the nanowire, the negative electric field drives Ag^+ ions through the insulating PVP encapsulation. Subsequent ion recrystallization forms a conductive bridge connecting the nanowire core to the electrode at electrode B. Conversely, at electrode A, the absence of a conductive channel between the other electrode and the nanowire results in high contact resistance, leading to the accumulation of joule heat. This thermal effect induces physical desorption of the PVP layer and triggers electromigration-induced welding at the contact end. Thus, this operational mode differentiates the electrode functions into the active end and the contact end.

To evaluate the stability of electrically formed contact and functional terminals, we designed a three-electrode test configuration by incorporating a third electrode (denoted as C) into the device architecture. High-voltage electroforming established direct core contacts at terminals A and C, bridging the Au electrodes to the Ag nanowire core. Terminal B constitutes the functional element, forming a metal-insulator-metal (MIM) structure with Au-PVP-Ag core layering.

To investigate temperature effects on PVP layer properties, we characterized device electrical performance under incremental annealing temperatures (Figure S2, Supporting Information).[39] Physical desorption has been shown to be a significant phenomenon at ≈100 °C, while contact has been observed to undergo partial enhancement, resulting in a reduction in V_{th}. Annealing at elevated temperatures has been shown to promote desorption, concurrently inducing PVP decomposition. This process does not induce a resistive state transition, exhibiting only negligible hysteresis. Following the annealing process at 200 °C, the decomposition of the PVP shell layer in proximity to the device electrodes facilitates the formation of a direct contact between the nanowires and the electrodes, transitioning the device to a persistent low-resistance state.

We characterized device electrical properties using a semiconductor analyzer to validate contact reliability. Figure 2b–d shows the *I*–*V* characteristics of different electrode pairs: (A-B) and (B-C) on the device under 0 V→1 V→0 V→−1 V→0 V voltage sweep. A 1 µA compliance current protected the device during testing. During forward biasing (0 V→1 V), the device maintains a high-resistance state (HRS) until ≈0.4 V, where current abruptly rises to compliance level, transitioning to a low-resistance state (LRS) for the remainder of the sweep. Reverse biasing

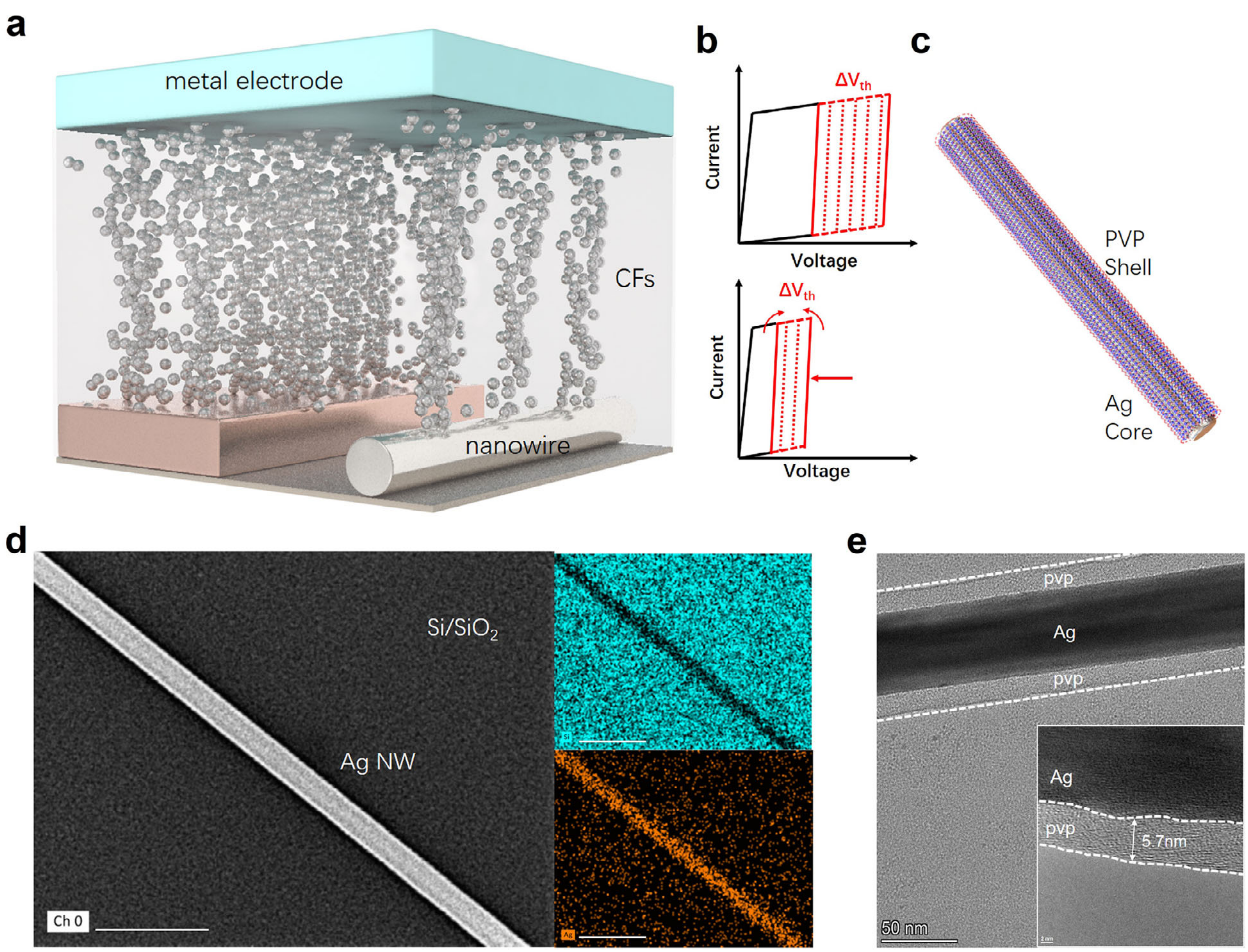

Figure 1. 1D silver nanowire memristor structure. a) A schematic representation of the limiting effect of using a 1D metal electrode on the growth of CF. b) A schematic diagram of threshold voltage fluctuation reduction by CF control. c) A schematic diagram of the silver nanowire structure, the nanowire diameters used in the experiments were 60 nm, and the length distribution varied from 5 to 20 µm. d) The elemental analysis by energy spectrometer of a single nanowire with a scale of 700 nm. e) Transmission electron microscopy (TEM) shows that the surface of the silver nanowire is covered with a 5–10 nm thick, irregular but continuous PVP layer.

(0 V→−1 V) exhibits identical switching behavior with symmetric threshold voltages concentrated at 0.4 V over multiple cycles. This bipolar threshold switching confirms conductive channel formation in the MIM structure. Figure 2c further demonstrates stable LRS establishment at terminals A and C, where direct Ag nanowire-electrode contacts yield minimal contact resistance during wide-voltage scans (±10 V), verifying contact stability. As shown in Figure 2e, the silver nanowire memristor demonstrates good consistency in the device-to-device variation test due to the stable shell PVP.

Bidirectional volatile switching occurs in symmetric-structure devices. At the functional terminal with asymmetric Ag-PVP-Au electrodes (Figure S3, Supporting Information), this phenomenon arises from silver atom accumulation forming conductive filaments near the Au electrode interface within the organic encapsulation layer. During Stage I (forward bias), field-driven Ag$^+$ ion migration from the Ag core toward the Au electrode establishes stable conductive pathways. Upon field removal, filament rupture occurs, with surface diffusion causing Ag cluster aggregation on both Ag core and Au electrode surfaces. During Stage III (negative bias), reverse migration of Ag clusters near the Au electrode reforms conductive pathways, enabling bidirectional volatile switching.

The device exhibits symmetric volatile switching behavior under low compliance current, as demonstrated by the bidirectional I-V characteristics in **Figure 3a**. During the forward voltage sweep from 0 to 0.5 V, the device remains in a high-resistance state (HRS) until the voltage reaches ≈0.4 V. At this threshold, a transition to the low-resistance state (LRS) occurs, constrained by a compliance current of 1 µA. This switching event features a steep activation slope of 12 mV dec^{-1}, indicating the onset of CF formation. As the voltage is swept back from 0.5 to 0 V, the device initially maintains the LRS. When the voltage drops to ≈0.2 V, the resistance sharply increases, restoring the original HRS. This transition suggests that the conductive filament spontaneously ruptures upon removal of the external electric field. A similar transition is observed during the reverse voltage sweep, confirming the symmetric and volatile nature of the switching behavior. Repetitive cycling over 200 test iterations confirm consistent switching near ±0.4 V (V_{th}), attributed to field-driven migration of Ag

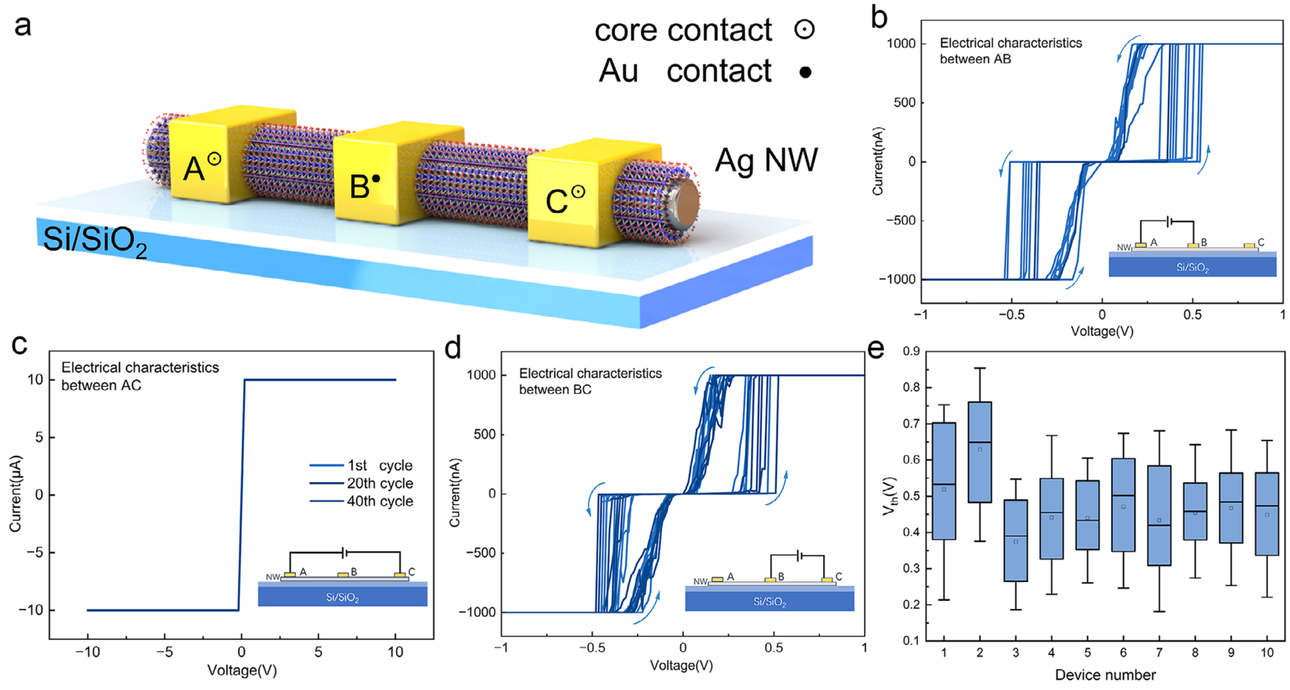

Figure 2. Structure characteristics of the NW memristor. a) Schematic diagram of the device with three contact areas A, B, and C. The contacts A and C are nuclear contacts connected to the inner core, and the contact B is located at the top of the PVP. b–d) *I–V* characteristics of the device with three different inter-electrode combinations. The inset in the figure shows the electrode combinations used for testing. e) Device-to-device distributions of V_{th} for the Ag NW memristors.

ions through the PVP layer and subsequent rupture via surface diffusion once the field is removed. The electrical characteristics of the device at different compliance currents can be found in Figure S4 (Supporting Information).

The device's switching thresholds are statistically confined, as shown in Figure 3b. Across 200 cycles, threshold voltages are distributed in the 0.22–0.67 V and −0.21–0.66 V ranges for forward and reverse directions, respectively. Coefficients of variation 14.3% (forward) and 14.9% (reverse) highlight relatively low cycle-to-cycle variability. The device exhibits exceptionally low power consumption. The static (standby) power is 50pW, calculated by $P_{\text{Standby}} = I_{\text{HRS}} \times V_{\text{read}}$, where $I_{\text{HRS}} = 500\text{pA}$ and $V_{\text{read}} = 0.1$ V. The dynamic (set) power consumption is calculated by $P_{\text{set}} = I_c \times V_{\text{set}}$, yielding 0.4 μW with $I_c = 1$ μA and $V_{\text{set}} = 0.4$ V. This combination of ultralow standby and operational power consumption, together with a high on/off resistance ratio exceeding 10^5, highlights the energy efficiency of the switching behavior. As further illustrated in Figure 3c, both resistance states become increasingly uniform over cycling, converging $\approx 10^{10}\Omega$(HRS) and $\approx 10^5\Omega$ (LRS), confirming the reliability of filament formation and rupture within the PVP-encapsulated silver nanowire structure.

As the current limit increases, the switching mode evolves. Figure 3d demonstrates that at 10, 100 nA, and 1 μA, the device consistently returns to HRS upon voltage removal, confirming volatile switching behavior under sub-microampere compliance. This behavior originates from insufficient filament stability at low current levels, which prevents CFs from persisting beyond the applied field. Consequently, increased threshold fluctuations and instability are observed. Above the 1 μA threshold, devices exhibit a transition toward nonvolatile switching. As indicated in Figure S5 (Supporting Information), the value of the compliance current I_C controls the device behavior, where switching becomes increasingly volatile as I_C is decreased.

Nonvolatile switching characteristics are confirmed at 1 mA compliance (Figure 3e). The device switches into LRS at ≈0.8 V and maintains this state until reset. Resetting requires a negative bias of ≈−0.8 V, with current limits removed. Two CF disruption mechanisms were observed. Under high current, a gradual reset process lowers current to the microampere level before returning to zero. Under lower currents (Figure S6, Supporting Information), the collapse is abrupt and leads to immediate HRS at −0.5 V, reflecting the fragility of thin CFs. Long-term retention data further validates device reliability. Figure 3f shows that both HRS ($\approx 10^{10}$ Ω) and LRS ($\approx 10^4$ Ω) remain stable across a 2k-second test and after a 24-h interval. No significant resistance drift or switching degradation is observed. This durability reflects the robust CF dynamics enabled by the core–shell nanowire structure and supports potential applications in crossbar arrays and neuromorphic circuits.

When operated in a volatile switching mode, the device exhibits zero sustaining voltage and spontaneously relaxes to HRS upon removal of the voltage sweep. Under low current-limit conditions, the device exhibited volatile switching behavior characterized by the inability to maintain a conductive state after voltage removal. This transient response originates not from a fundamentally different switching mechanism but from a reduced CF lifetime. Previous studies suggest[40–42] that both volatile and nonvolatile switching modes stem from the same filamentary dynamics, with the key distinction arising from differences in

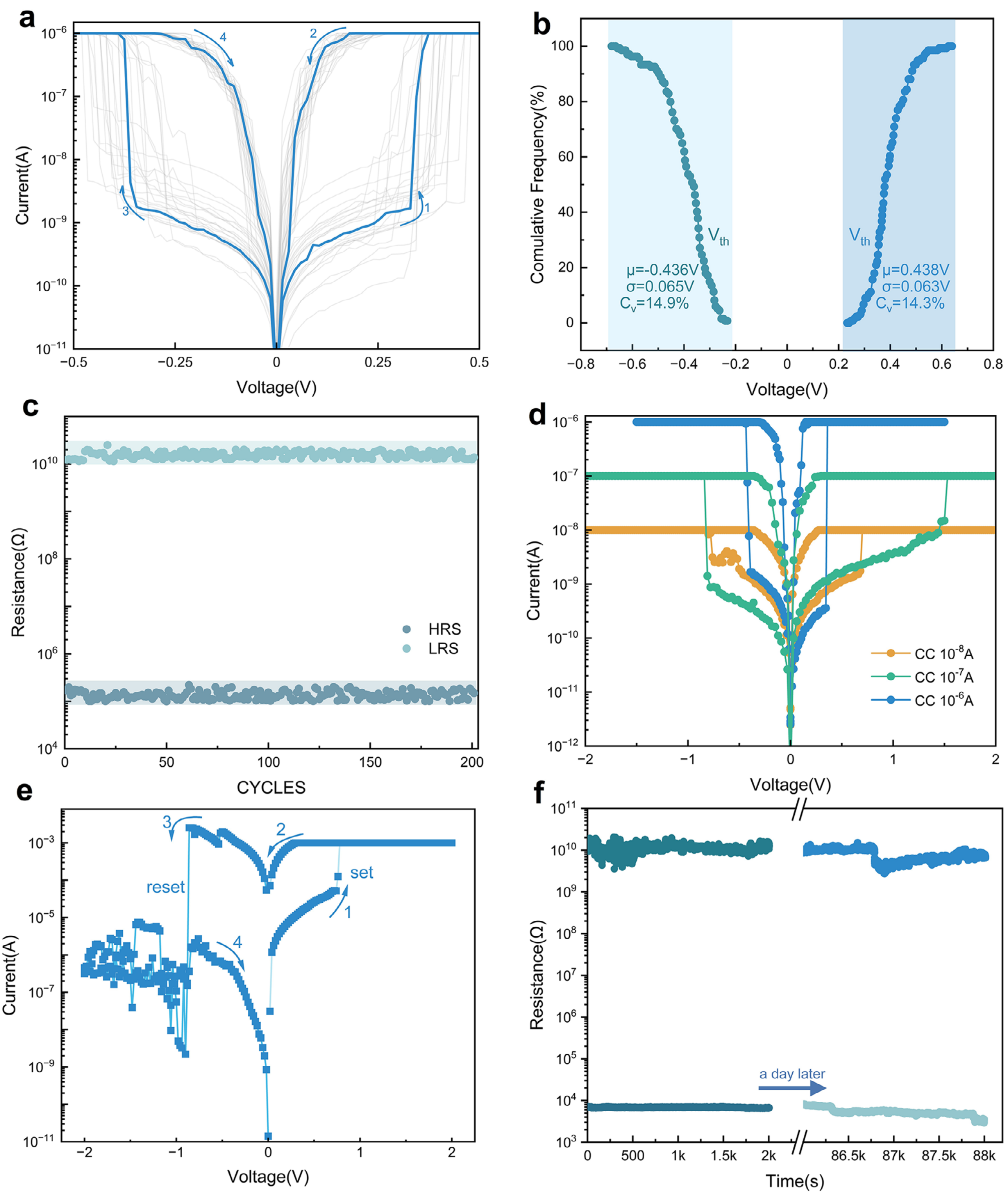

Figure 3. Electrical characteristics of the NW memristor. a) Bidirectional volatile switching of the device over a scan voltage range of −0.5 to 0.5 V in logarithmic scale. Voltage sweep paths are shown from 1 to 4. b) Cumulative probability distribution of the threshold voltage with coefficients of variation of 14.9% and 14.3%, respectively. c) Resistance distribution of the device in high and low resistance states over 200 test cycles at $V_{read} = 0.1$ V. d) Typical *I–V* curves of the device at different compliance current (CC). e) Nonvolatile RS mode of the device at high limiting current. f) Retention characteristics of the HRS and LRS of the nonvolatile device for up to 88000 seconds at a 0.1 V read voltage.

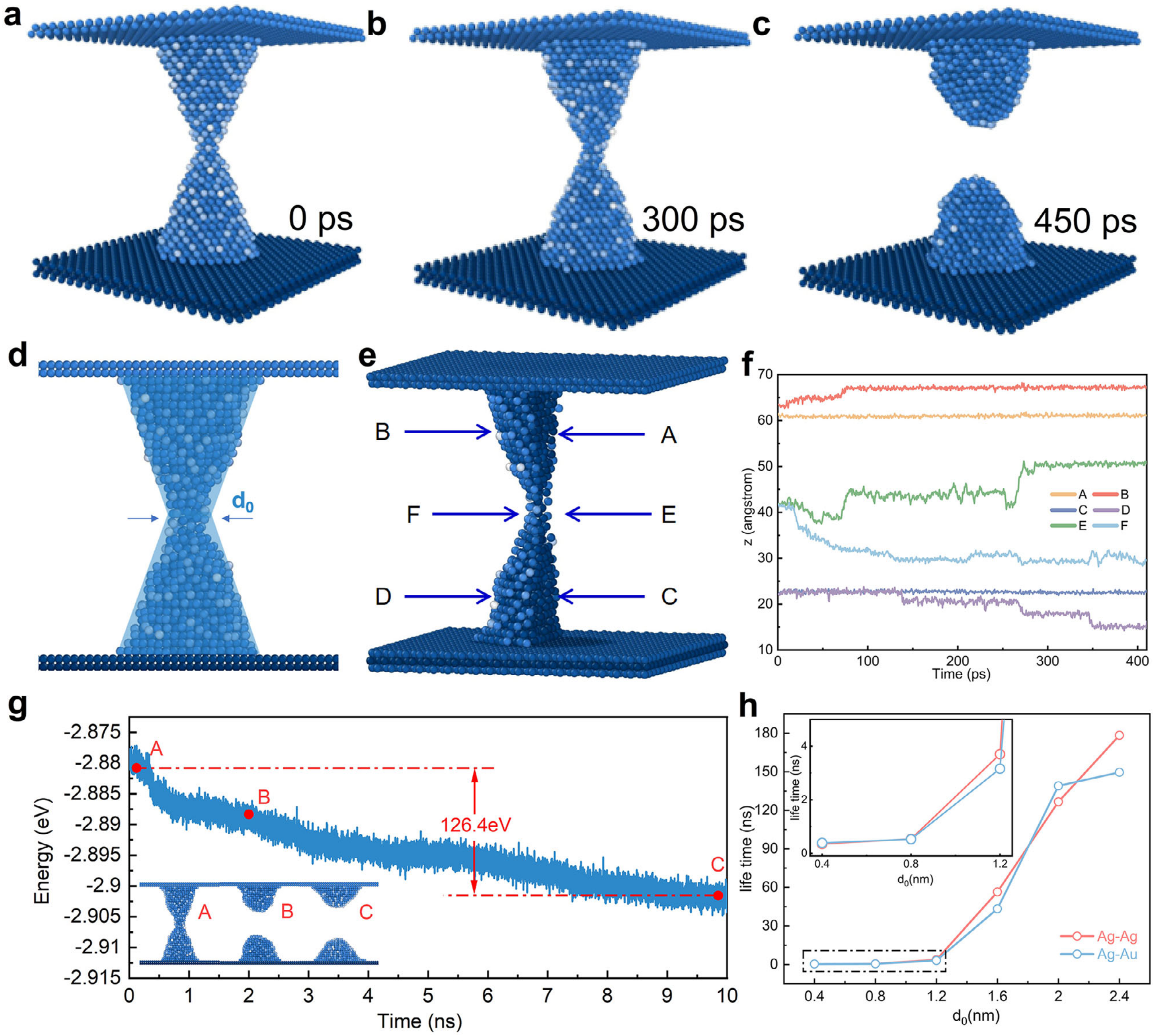

Figure 4. MD simulation of surface diffusion. a–c) MD simulation results of Ag nanoscale CF between two electrode plates for three periods of time at $t = 0$, 300 ps and 450 ps. d) Conducting filament model and bottleneck region diameter markers used for simulation. e,f) Cross-sectional view of CF at 100 ps and typical trajectories of individual atoms along the z-direction in which block atoms (A,C), surface atoms (B,D) and bottleneck atoms (E,F) are located. g) The following observations were made on the energy relaxation of the MD-simulated filaments: the total energy evolution curve with simulation time was measured. h) Filament lifetime as a function of normalized diameter for different electrode materials.

thermodynamic stability and filament persistence. Metal CF lifetimes are found to be strongly influenced by the self-diffusion of surface atoms.[43–45] Gradients in the concentration of surface atomic vacancies have been shown to lead to the migration of atoms on the CF surface in the direction of surface area minimization. This, in turn, has been demonstrated to result in the aggregation of metal atoms and, ultimately, to CF rupture. Moreover, recent in situ transmission electron microscopy (TEM)[46,47] observations demonstrate that Ag and Cu atoms from conducting filaments exhibit a propensity to form clusters without diffusing into the dielectric material.

To clarify the rupture mechanism, molecular dynamics (MD) simulations were conducted using the embedded atom method (EAM) to investigate atomic-scale evolution driven by surface diffusion. The simulation model consisted of a silver filament positioned between a gold top electrode and a silver bottom electrode, mimicking the vertical configuration of nanowire-based memristors. The system temperature was set to 800 K to accelerate morphological changes. As shown in **Figure** 4a–c, a narrow conductive neck with a diameter of ≈0.4 nm forms at 0 ps under an applied electric field. By 300 ps, significant atomic mobility is observed at the filament surface, initiating structural deformation. At 450 ps, the filament completely ruptures, separating into two discrete silver clusters anchored at the respective electrode interfaces. The geometric model is illustrated in Figure 4d, comprising two truncated cones joined at the narrowest point (d_0), where rupture is initiated.

Figure 4e,f reveals the spatial mobility of individual atoms within the filament structure. Atoms A and C, located in the inner filament core, remain nearly stationary over 450 ps. In contrast, surface atoms B and D migrate toward the electrodes, gradually destabilizing the structure. Bottleneck atoms E and F exhibit lateral displacement, ultimately resulting in filament disintegration. These results indicate that surface-driven atomic diffusion is the primary mechanism underlying filament instability, consistent with classical models based on chemical potential gradients.[48]

Figure 4g provides a quantitative analysis of potential energy evolution during filament rupture. At point A, the applied electric field induces neck formation, causing a slight increase in system energy due to tensile strain. At point B, the onset of surface atom rearrangement leads to a sharp energy drop of ≈126.4 eV, signifying filament breakage. By point C, the system reaches a stable state, forming two isolated Ag clusters, and the total energy plateaus. These transitions confirm that spontaneous filament rupture is energetically favorable and driven by surface diffusion.

To investigate the size dependence of filament stability, filaments with bottleneck diameters ranging from 0.4 to 2.4 nm were simulated. The results reveal that increasing the bottleneck diameter markedly prolongs rupture time, demonstrating a strong size-dependent stability. As shown in Figure 4h, filament lifetime increases nonlinearly with the bottleneck diameter. For $d_0 = 2$ nm, the filament lifetime reaches 180 ns. This trend is consistent across both gold-silver and silver-silver electrode systems, validating that memristive switching mechanisms are fundamentally similar between single nanowire devices and their networked counterparts. Additional simulations using symmetric Ag electrodes (Figures S7–S9, Supporting Information) further corroborate this conclusion.

Injury receptors, a critical subclass of sensory receptors, are specialized to detect noxious external stimuli and trigger protective motor responses via action potentials transmitted to the central nervous system (**Figure** 5a).[49–51] This process serves to minimize physical damage by activating only when stimuli exceed a defined threshold. Unlike most sensory receptors, injury receptors exhibit no adaptation to sustained stimuli; their sensitivity does not decrease over time. Upon exposure to excessively intense stimuli that cause tissue damage, these receptors undergo sensitization, characterized by a lowered response threshold and heightened output intensity—phenomena known as nociceptive hypersensitivity and anomalous pain, respectively (Figure 5b).[52–55]

To emulate this behavior in a nanowire memristive device, electrical pulses with varying amplitudes, durations, and counts were applied as external stimuli. When a 50 ms pulse was applied (Figure 5c), the device remained in an inactive state until the pulse amplitude reached 0.8 V, at which point it exhibited a current of ≈800 nA. Beyond this threshold, further increases in amplitude induced a sharp rise in current, mimicking biological activation. A sufficient interval between individual tests ensured that the device returned to equilibrium before each measurement.

Using a fixed amplitude of 1 V, the current response became stable as the pulse width reached 40 ms, and both current magnitude and duration further increased at 50 ms (Figure 5d). This response parallels the biological relationship between stimulus duration and perceived pain intensity. Additionally, the current response depended on the number of applied pulses. Repeated stimulation with 50 ms pulses of increasing voltage (Figures S10 and S11, Supporting Information) revealed that the output current stabilized after initial fluctuations. CF formation, influenced by pulse duration and strength, established a stable connection between the top electrode and the nanowire core. Once formed, this CF maintained a consistent current response regardless of continued stimulation. This non-adaptive behavior resembles the maladaptive characteristic of biological injury receptors, which persistently fire in response to prolonged noxious input.

The process of eliminating a noxious stimulus so that the signal from the damaged receptors in the body disappears is termed "relaxation". As demonstrated in Figure 5e, an activation pulse with an amplitude of 1 V and a pulse width of 50 ms is initially applied to the device to facilitate its conductivity. Subsequently, a read pulse (0.6 V, 50 ms) is applied, and the current response of the device is recorded after various intervals of 10–200 ms. This relaxation process is analogous to that of biological injury receptors, which require a period of time to return to their undamaged state following trauma.

Sensitization in biological nociceptors is a protective response that enhances receptor sensitivity post-injury. This behavior comprises two key nociceptive phenomena: nociceptive hypersensitivity manifested as exaggerated pain response to noxious stimulation, and allodynia presenting as pain perception triggered by normally nonpainful stimulation. These phenomena were successfully replicated in the device using pre-damaging pulses at 2 and 3 V magnitudes, followed by stimulus pulses with amplitudes ranging from 0.4 to 1.2 V. The current response was recorded over 30 s after the initial injury pulse (Figure 5f). Devices in the sensitized state showed elevated current responses, which scaled with the degree of prior damage (Figure 5g). For a 1 V test pulse, the current rose from 56 μA (undamaged) to 230 and 480 μA after 2 and 3 V injuries, respectively. Furthermore, the device's threshold voltage shifted to lower values (Figure 5h), indicating enhanced sensitivity akin to biological nociceptors. This behavior closely mirrors the pathological characteristics of sensitized pain perception.

3. Conclusion

We have developed a core–shell silver nanowire-based memristor that achieves precise spatial confinement of conductive filament growth through a fabrication-friendly architecture. This 1D structure, consisting of a conductive Ag core and an ultrathin PVP shell, enables highly uniform and energy-efficient switching behavior. The device exhibits a low threshold voltage (0.22 V), excellent switching consistency (coefficient of variation <15%), and ultralow power consumption (≈400 pW), addressing key limitations of stochastic filament formation in filamentary memristors. Molecular dynamics simulations elucidate the mechanism of filament rupture and correlate filament dimensions with

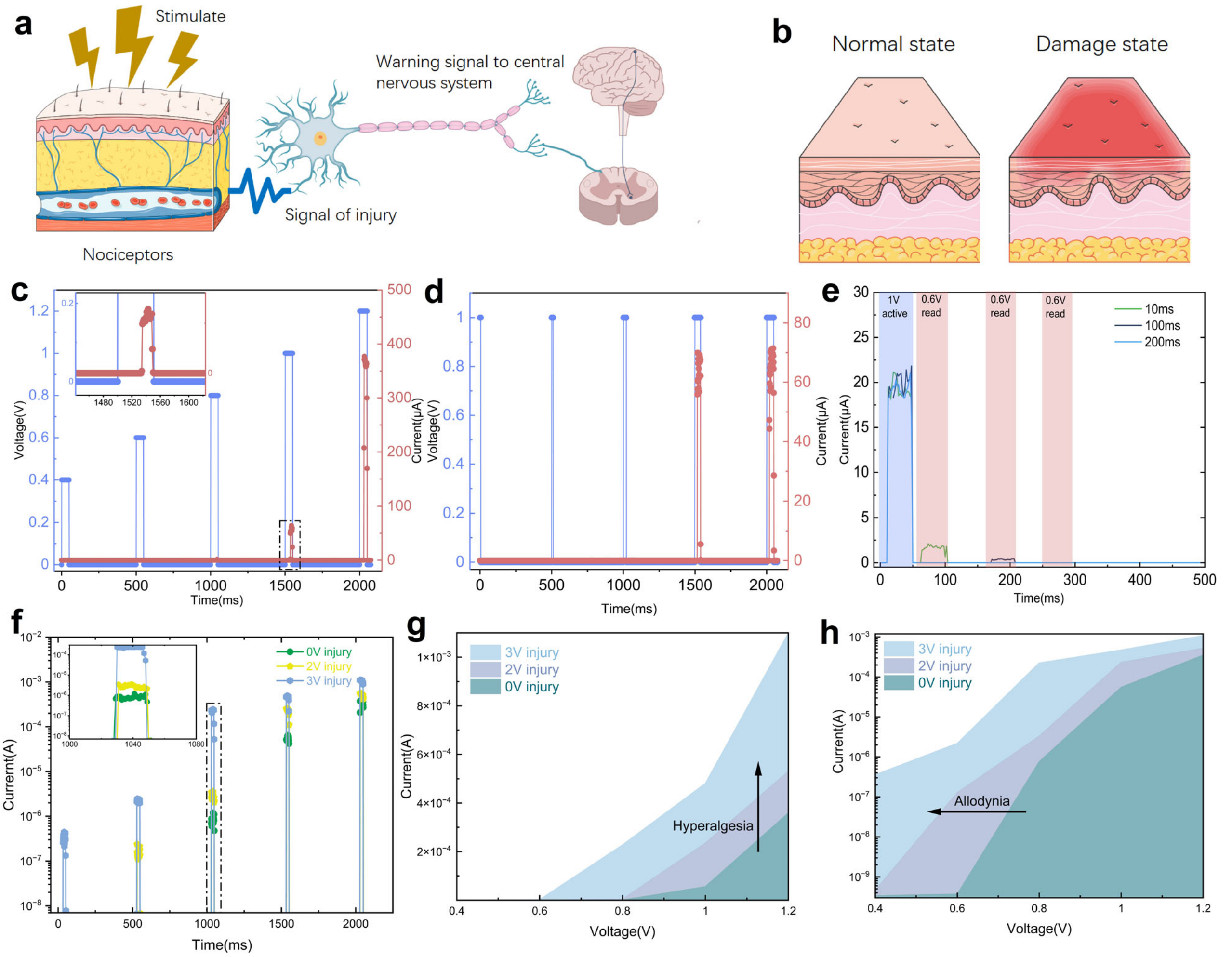

Figure 5. Nociceptive characteristics of the NW device. a) When the body is subjected to a noxious stimulus, the receptors produce the sensation of pain and transmit it to the nerve centre. The injury receptor system in the body corresponds to the artificial injury receptor circuit consisting of a diffusion memristor (threshold switch). b) Schematic representation of the injury state and the normal state of the receptor presented by an overstimulated receptor. c) A series of 50 ms voltage pulses and output currents having different amplitudes (0.4, 0.6, 0.8, 1, and 1.2 V) and corresponding output currents. d) A sequence of 1 V pulses with different pulse widths (5, 10, 20, 40, and 50 ms) and corresponding output currents. e) Output current under 1 V excitation for 50 ms, considering different recovery times of the device. f) Average output currents with 0.4, 0.6, 0.8, 1, or 1.2 V pulse amplitudes applied 1 min after a 0, 2, or 3 V injury pulse. g,h) Receptor anomalous pain and nociceptive hypersensitivity embodied by the current characteristics of the injured device.

temporal stability, offering insight into the intrinsic volatile switching behavior. Importantly, the device replicates essential nociceptor-like functionalities, including threshold-triggered activation, relaxation, and sensitization, further enhancing its relevance for neuromorphic systems. This work presents a universal and scalable structural platform that achieves deterministic CF regulation through a minimalist yet robust design. Its compatibility with diverse materials and ease of integration position it as a foundational approach for next-generation neuromorphic, flexible, and crossbar-integrated memory systems.

4. Experimental Section

Au/PVP/Ag NW Memristors Fabrication: Silver nanowires (length: 10 µm, diameter: 60, 120 nm) were purchased from XFNANO Co., ltd. Ag NWs (0.1 mL) solution was added to ethanol (10 mL) to form the blended solution. The resultant solution was spin-coated onto the 285 nm SiO_2/Si substrate at 1000 rpm for 45 s, and then evaporated for 15 min at room temperature. The patterning of the electrodes was achieved by electron beam lithography with positive photoresist. After exposure and development, 10/30 nm Cr/Au electrodes were deposited via electron beam evaporation. Finally, the device was completed after a standard lift-off process.

Material Characterization and Electrical Measurement: The atomic force microscopy (AFM) image was acquired using the Bruker Dimension Icon, while the PVP Shell Thickness Information was obtained with in-situ STM-TEM electrical measurement system. Electrical characteristics were measured under ambient conditions using an Agilent B1500A semiconductor parameter analyzer with a B1525A (HV-SPGU) module and Metatest E2 photoelectric testing system.

MD Simulation: All the MD simulations were performed by the LAMMPS program. The interactions between Ag atoms were described by the EAM potential. Nose–Hoover NVT ensemble was used, and the system temperature was set to 800 K to observe the fusing of the filament in a reasonable simulation time. The MD simulations are carried out in an $8.18 \times 8.18 \times 9.00$ nm^3 box, with periodical boundary conditions in the *x*- and *y*-axes and fixed boundary conditions in the *z*-axis. For the case where the upper and lower plates are both silver electrodes, two/three fixed layers of Ag atoms at the top/bottom of the box act as the top/bottom electrodes. For the case where the upper plate is a silver electrode and the lower plate is a gold electrode, the three layers of Ag atoms were replaced by three layers of Au atoms. The initial atomic structure of the filament consists of two cones cut from the bulk Ag crystal. Filaments with different diameters (*d*), ranging from 0.4 to 2.4 nm, were constructed to explore the relationship between lifetime and diameter. Due to the stochastic nature of filament melting, multiple sets of MD simulations for each size of filament were performed. The lifetime of the filament is given by the average value. For $d = 0.4$, 0.8, and 1.2 nm, 10 sets of MD simulations were performed. For $d = 1.6$, 2.0, and 2.4 nm, 5 sets of MD simulations were performed.

Supporting Information

Supporting Information is available from the Wiley Online Library or from the author.

Acknowledgements

This study was supported by the National Science Foundation of China (Grant Nos. 62304151, 62204170, and 62474124), the Natural Science Foundation of Tianjin (Grant No. 22JCQNJC01010), the open research of Songshan Lake Materials Laboratory (Grant No. 2023SLABFK07), the China Postdoctoral Science Foundation (No. 2023M742585), the State Key Laboratory of Fluid Power and Mechatronic Systems under Grant No. GZKF-202327, the State Key Laboratory of Mechanics and Control for Aerospace Structures (Nanjing University of Aeronautics and Astronautics) (Grant No. MCMS-E-0123Y01), and the Open Project of State Key Laboratory of Transducer Technology (Grant No. SKT2208).

Conflict of Interest

The authors declare no conflict of interest.

Data Availability Statement

The data that support the findings of this study are available from the corresponding author upon reasonable request.

Keywords

Ag nanowires, high switching uniformity, memristor, nociceptor-like functionalities, spatial confinement

Received: July 21, 2025
Revised: August 17, 2025
Published online:

[1] Y. Chen, Y. Huang, Q. Li, Z. Luo, Z. Zhang, H. Huang, J. Sun, L. Zhang, R. Sun, D. J. Bain, J. F. Conway, B. Lu, S. Li, *Nat. Nanotechnol.* **2023**, *18*, 193.
[2] A. John-Herpin, D. Kavungal, L. von Mücke, H. Altug, *Adv. Mater.* **2021**, *33*, 2006054.
[3] S. H. Sung, N. Schnitzer, S. Novakov, I. El Baggari, X. Luo, J. Gim, N. M. Vu, Z. Li, T. H. Brintlinger, Y. Liu, W. Lu, Y. Sun, P. B. Deotare, K. Sun, L. Zhao, L. F. Kourkoutis, J. T. Heron, R. Hovden, *Nat. Commun.* **2022**, *13*, 413.
[4] M. A. Zidan, J. P. Strachan, W. D. Lu, *Nat. Electron* **2018**, *1*, 22.
[5] G. J. Fan, L. H. Sun, L. Meng, C. Hu, X. Wang, Z. Shi, C. Hu, Y. Han, Q. Yang, L. Cao, X. Zhang, Y. Zhang, X. Song, S. Xia, B. He, S. Zhang, C. Wang, *Nat. Commun.* **2021**, *12*, 20.
[6] F. Cao, Z. J. Hu, T. T. Yan, E. Hong, X. Deng, L. Wu, X. Fang, *Adv. Mater.* **2023**, *35*, 2304550.
[7] T. P. Ko, Y. C. Wang, C. S. Yang, M.-H. Hou, C.-J. Chen, Y.-F. Chiu, Y. Chen, *Nat. Commun* **2022**, *13*, 26.
[8] W. Li, Y. Yan, Y. Y. Gong, J. Cai, F. Cai, R. S. Gurney, D. Liu, A. J. Pearson, D. G. Lidzey, T. Wang, *Adv. Funct. Mater* **2018**, *28*, 1704212.
[9] X. Chen, B. Chen, B. Jiang, T. Gao, G. Shang, S.-T. Han, C.-C. Kuo, V. A. L. Roy, Y. Zhou, *Adv. Funct. Mater* **2023**, *33*, 2208807.
[10] X. Chen, B. K. Chen, P. F. Zhao, V. A L Roy, S.-T. Han, Y. Zhou, *Mater. Futures* **2023**, *2*, 023501.
[11] R. R. Fang, W. Y. Zhang, K. Ren, K. Ren, P. Zhang, X. Xu, Z. Wang, D. Shang, *Mater. Futures* **2023**, *2*, 022701.
[12] S. K. Hwang, S. Y. Min, I. Bae, S. M. Cho, K. L. Kim, T.-W. Lee, C. Park, *Small* **2014**, *10*, 1976.
[13] R. Shen, Y. F. Jiang, Z. W. Li, J. Tian, S. Li, T. Li, Q. Chen, *Materials* **2022**, *15*, 8247.
[14] D. Wang, B. A. Sheriff, M. McAlpine, J. R. Heath, *Nano Res.* **2008**, *1*, 9.
[15] S. I. Kim, J. H. Lee, Y. W. Chang, S. S. Hwang, K.-H. Yoo, *Appl. Phys. Lett.* **2008**, *93*, 033503.
[16] S. W. Lee, J. M. Kim, W. Park, H. Lee, G. R. Lee, Y. Jung, Y. S. Jung, J. Y. Park, *Nat. Commun.* **2021**, *12*, 40.
[17] G. Milano, S. Porro, I. Valov, C. Ricciardi, *Adv. Electron. Mater* **2019**, *5*, 1800909.
[18] Z. Zhou, C. Lan, R. Wei, J. C. Ho, *J. Mater. Chem. C* **2019**, *7*, 202.
[19] X. Guo, Q. Wang, X. Lv, H. Yang, K. Sun, D. Yang, H. Zhang, T. Hasegawa, D. He, *Nanoscale* **2020**, *12*, 4320.
[20] C. C. Hsu, S. Y. Hua, X. Z. Zhang, X.-Z. Zhang, W.-C. Jhang, C.-W. Cheng, J.-E. Tsai, Y.-M. Wu, Y.-S. Chien, W.-C. Wu, *J. Alloys Compd* **2022**, *898*, 162918.
[21] D. K. Lee, G. H. Kim, H. Sohn, M. K. Yang, *Phys. Status Solidi-R* **2020**, *14*, 1900646.
[22] K. Park, J. S. Lee, *Nanotechnology* **2016**, *27*, 125203.
[23] S. Rehman, J. H. Hur, D. K. Kim, *J. Phys. Chem. C* **2018**, *122*, 11076.
[24] J. H. Yoon, S. Yoo, S. J. Song, K. J. Yoon, D. E. Kwon, Y. J. Kwon, T. H. Park, H. J. Kim, X. L. Shao, Y. Kim, C. S. Hwang, *ACS Appl. Mater. Interfaces* **2016**, *8*, 18215.
[25] S. Z. Liu, J. M. Zeng, Z. X. Wu, H. Hu, A. Xu, X. Huang, W. Chen, Q. Chen, Z. Yu, Y. Zhao, R. Wang, T. Han, C. Li, P. Gao, H. Kim, S. J. Baik, R. Zhang, Z. Zhang, P. Zhou, G. Liu, *Nat. Commun.* **2023**, *14*, 7655.
[26] Z. Y. Lv, S. R. Zhu, Y. Wang, Y. Ren, M. Luo, H. Wang, G. Zhang, Y. Zhai, S. Zhao, Y. Zhou, M. Jiang, Y.-B. Leng, S.-T. Han, *Adv. Mater.* **2024**, *36*, 2405145.
[27] J. Qiu, J. Li, W. Li, K. Wang, S. Zhang, C. H. Suk, C. Wu, X. Zhou, Y. Zhang, T. Guo, T. W. Kim, *ACS Nano* **2024**, *18*, 31632.
[28] Y. H. Ting, J. Y. Chen, C. W. Huang, T.-K. Huang, C.-Y. Hsieh, W.-W. Wu, *Small* **2018**, *14*, 1703153.
[29] R. Yadav, S. Poudyal, B. Biswal, R. Rajarapu, P. K. Barman, K. S. Novoselov, A. Misra, *Appl. Phys. Lett.* **2024**, *125*, 213504.
[30] Y. J. Li, J. S. Tang, B. Gao, W. Sun, Q. Hua, W. Zhang, X. Li, W. Zhang, H. Qian, H. Wu, *Adv. Sci.* **2020**, *7*, 2002251.
[31] W. Xiao, W. Song, Y. P. Feng, D. Gao, Y. Zhu, J. Ding, *J. Mater. Chem. C* **2020**, *8*, 1577.
[32] B. K. You, J. M. Kim, D. J. Joe, K. Yang, Y. Shin, Y. S. Jung, K. J. Lee, *ACS Nano* **2016**, *10*, 9478.
[33] W. Dang, Y. Shen, W. Wei, C. Pan, F. Chen, G.-J. Ruan, Y. Luo, Y. Guo, Q. Tan, J. Shi, X.-J. Yangdong, S. Chen, C. Wang, Y. Xie, Z.-Z. Yang, P. Wang, S. Wang, L.i Zhong, S. Cheng, C. Zhu, B. Cheng, S.-J. Liang, F. Miao, *Sci. Adv.* **2025**, *11*, 3309.

[34] Z. S. Li, J. Q. Wang, L. X. Xu, L. Wang, H. Shang, H. Ying, Y. Zhao, L. Wen, C. Guo, X. Zheng, *Adv. Mater.* **2024**, *36*, 2308843.
[35] A. Kumar, L. Huang, L. Hu, D. Yin, H. Lin, M. T. Swihart, *J. Mater. Chem. A* **2021**, *9*, 12755.
[36] J. Qiu, J. Li, W. Li, K. Wang, T. Xiao, H. Su, C. H. Suk, X. Zhou, Y. Zhang, T. Guo, C. Wu, P. C. Ooi, T. W. Kim, *ACS Appl. Mater. Interfaces* **2024**, *16*, 10361.
[37] H. Xu, Z. Chen, S. Hao, K. A. Fichthorn, B. J. Wiley, *Nanoscale* **2023**, *15*, 5219.
[38] J. L. Cui, X. Y. Ren, X. S. Mei, Z. Fan, C. Huang, Z. Wang, X. Sun, W. Wang, *Int. J. Extreme Manuf.* **2023**, *5*, 025503.
[39] Y. Zhu, J. Chen, T. Wan, S. Peng, S. Huang, Y. Jiang, S. Li, D. Chu, *ACS Appl. Electron. Mater.* **2019**, *1*, 1275.
[40] A. Bricalli, E. Ambrosi, M. Laudato, M. Maestro, R. Rodriguez, D. Ielmini, *IEEE Trans. Electron Devices* **2018**, *65*, 122.
[41] B.-G. Chae, J.-B. Seol, J.-H. Song, K. Baek, S.-H. Oh, H. Hwang, C.-G. Park, *Adv. Mater.* **2017**, *29*, 1701752.
[42] X. Zhao, H. Xu, Z. Wang, L. Zhang, J. Ma, Y. Liu, *Carbon* **2015**, *91*, 38.
[43] H. W. Sheng, M. J. Kramer, A. Cadien, T. Fujita, M. W. Chen, *Phys. Rev. B* **2011**, *83*, 134118.
[44] N. Shukla, R. K. Ghosh, B. Grisafe, S. Datta, presented at IEEE International Electron Devices Meeting (IEDM), IEEE, San Francisco, CA, USA **2017**.
[45] M. Wang, W. Wang, W. R. Leow, C. Wan, G. Chen, Y. Zeng, J. Yu, Y. Liu, P. Cai, H. Wang, D. Ielmini, X. Chen, *Adv. Mater.* **2018**, *30*, 1802516.
[46] Z. Wang, S. Joshi, S. E. Savel'ev, H. Jiang, R. Midya, P. Lin, M. Hu, N. Ge, J. P. Strachan, Z. Li, Q. Wu, M. Barnell, G.-L. Li, H. L. Xin, R. S. Williams, Q. Xia, J. J. Yang, *Nat. Mater.* **2017**, *16*, 101.
[47] F. Yuan, Z. Zhang, C. Liu, F. Zhou, H. M. Yau, W. Lu, X. Qiu, H.-S. P. Wong, J. Dai, Y. Chai, *ACS Nano* **2017**, *11*, 4097.
[48] W. Wang, M. Wang, E. Ambrosi, A. Bricalli, M. Laudato, Z. Sun, X. Chen, D. Ielmini, *Nat. Commun.* **2019**, *10*, 81.
[49] A. I. Basbaum, D. M. Bautista, G. Scherrer, D. Julius, *Cell* **2009**, *139*, 267.
[50] A. E. Dubin, A. Patapoutian, *J. Clin. Invest.* **2010**, *120*, 3760.
[51] C. J. Woolf, Q. F. Ma, *Neuron* **2007**, *55*, 353.
[52] A. Latremoliere, C. J. Woolf, *J. Pain* **2009**, *10*, 895.
[53] M. S. Gold, G. F. Gebhart, *Nat. Med.* **2010**, *16*, 1248.
[54] D. M. Cain, S. G. Khasabov, D. A. Simone, *J. Neurophysiol.* **2001**, *85*, 1561.
[55] V. Neugebauer, W. D. Li, *J. Neurophysiol.* **2002**, *87*, 103.